Los Alamos
NATIONAL LABORATORY
EST.1943

LA-UR-13-27175
Approved for public release; distribution is unlimited.

Title: Strain Partitioning in Ultra-Fine Grained Medium-Manganese Transformation Induced Plasticity Steel

Author(s):
Gibbs, Paul J.
De Cooman, Bruno
Brown, Donald W.
Clausen, Bjorn
Schroth, James G.
Merwin, Matthew J.
Matlock, David K.

Intended for: Materials Science and Engineering A

Issued: 2014-08-12 (rev.3)

Disclaimer:
Los Alamos National Laboratory, an affirmative action/equal opportunity employer,is operated by the Los Alamos National Security, LLC for the National NuclearSecurity Administration of the U.S. Department of Energy under contract DE-AC52-06NA25396. By approving this article, the publisher recognizes that the U.S. Government retains nonexclusive, royalty-free license to publish or reproduce the published form of this contribution, or to allow others to do so, for U.S. Government purposes. Los Alamos National Laboratory requests that the publisher identify this article as work performed under the auspices of the U.S. Departmentof Energy. Los Alamos National Laboratory strongly supports academic freedom and a researcher's right to publish; as an institution, however, the Laboratory does not endorse the viewpoint of a publication or guarantee its technical correctness.

Strain Partitioning in Ultra-Fine Grained Medium-Manganese Transformation Induced Plasticity Steel

P.J. Gibbs[a,b,1]*, B.C. De Cooman[c], D.W. Brown[b,d], B. Clausen[d], J.G. Schroth[e], M.J. Merwin[f], and D.K. Matlock[a]

a Advanced Steel Processing and Products Research Center, Colorado School of Mines, Golden CO
b Materials Science and Technology Division, Los Alamos National Laboratory, Los Alamos NM
c Graduate Institute of Ferrous Technology, Pohang University of Science and Technology Pohang, South Korea
d Los Alamos Neutron Science Center, Los Alamos National Laboratory, Los Alamos NM
e Research and Development Center, General Motors Corp., Warren, MI
f United States Steel Research and Technology Center, Munhall PA

1 Paul Gibbs performed this work as a graduate research assistant at the Colorado School of Mines and is now a post-doctoral research associate at Los Alamos National Laboratory

***Corresponding author: pgibbs@lanl.gov**

ABSTRACT

A 7.1-Mn 0.1-C transformation-induced plasticity steel was intercritically annealed at 600 °C and 650 °C for 168 hours. Ultra-fine-grained microstructures with annealing temperature dependent retained austenite fractions and tensile properties were produced. *In situ* neutron diffraction was used to investigate the change in tensile properties *via* measurement of phase fractions, elastic phase strains, and diffraction peak broadening during deformation. Austenite transformation to martensite controlled initial yielding in the 650 °C annealed steel and stress induced transformation was observed. In contrast, yielding after annealing at 600 °C was controlled by plastic deformation of ferrite, with austenite transformation initiating only after yield point elongation. The sequence of deformation between constituents was readily apparent in the lattice strain and peak width data. During deformation, compressive lattice strains were always developed in austenite, ferrite plastic deformation initiated around 700 MPa in both steels, and tensile stress was preferentially transferred to deformation-induced martensite. The development of compressive strains in austenite was related to constraint of the volume expansion during austenite transformation to martensite.

1.0 INTRODUCTION

Intercritical annealing of medium-manganese (Mn) (*i.e.* 5 to 10 wt pct. Mn), low carbon, transformation-induced plasticity (TRIP) steels is an effective methodology to make steels of interest to meet third generation advanced high strength steel (AHSS) properties goals [1,2]. During annealing in the two-phase ferrite and austenite region, enrichment of Mn to austenite from ferrite stabilizes austenite to room temperature on subsequent cooling [3,4]. The annealing temperature controls the relative Mn-enrichment of austenite and thereby determines the subsequent austenite stability during deformation. Previous work employing this processing methodology [5–14] has highlighted the potential to produce high tensile strength and ductility combinations through systematic variations in heat treatment methods, intercritical annealing temperature, and retained austenite content. The resulting properties clearly correlate with variations in austenite stability [3,13,14]; however, the fundamental interactions between phases during deformation and austenite transformation to martensite have received limited attention.

In situ neutron diffraction provides a method to directly monitor lattice plane spacings in multiple phases as a function of applied stress and/or strain during deformation, and thus is attractive as a method for investigating deformation. Small changes in interplanar spacing serve as microstructurally scaled internal ‘strain gauges’ to monitor deformation in crystalline materials. In multiphase materials, differences between material properties (*e.g.* elastic modulus, yield stress, or work hardening rate) of the constituent phases result in a divergence between the lattice strains of individual phases with deformation. Three distinct regimes of deformation in a two phase composite may be defined [15]: Stage 1 deformation where both phases deform reversibly, resulting in bulk linear and elastic loading; Stage 2 deformation is marked by the initiation of plastic flow in the lower strength constituent, the elastic lattice strain of each phase continues to increase, however, changes in the stress on each phase due to yielding of the ‘soft’

phase results in a decrease in the slope of the stress-lattice strain relation for the 'hard' phase and increase in the slope of the 'soft' phase; Stage 3 deformation occurs when the 'hard' phase also deforms plastically resulting in work hardening rate dependent stresses in each phase and corresponding changes in the lattice strains. Observations of stress loci for changes in the slope of the lattice strain-applied stress behavior yield valuable information about the sequence in which various constituents yield plastically and the influence of the flow strength of individual constituents on the mechanical properties of the multiphase microstructure [15,16].

TRIP steels present a special situation when considering lattice strain partitioning effects due to the dynamic transformation of austenite to martensite with deformation. As austenite is replaced by martensite, the physical force on austenite will decrease, however this decrease may not be proportionate to the change in austenite volume fraction due to the load redistribution to the hard martensite, and the resulting changes in the stress applied to austenite. Additionally, the large volume change (approximately 3 pct.) and lattice shear associated with the diffusion-less austenite to α' martensite transformation will also affect the elastic lattice strains [17,18]. Previous *in situ* diffraction studies of lattice strains in TRIP steels have highlighted results that are highly sensitive to the specific processing methodology, austenite morphology, and matrix microstructure studied [19,20]. Diverse experimental results are reported and vary from lattice strains being preferentially transferred to austenite as a 'hard' phase after the onset of plastic deformation [19,21–23] to a slight austenite relaxation after the onset of transformation [15,24].

In the present study, *in situ* neutron diffraction was performed on a 7.1Mn-0.1C sheet steel to provide direct measurement of mechanical interactions between constituent phases by recording the phase-specific elastic lattice strains during uniaxial tensile deformation on samples heat treated to produce significantly different austenite stability conditions. The observed

differences in macroscopic yielding and work hardening are related to changes in the austenite transformation mechanism in each alloy. The sequence of deformation between phases explains the work hardening behavior observed in ultra fine-grained Mn-TRIP steels.

2.0 EXPERIMENTAL METHODS AND MATERIALS

The experimental steel with the composition of 0.099C-7.09Mn-0.13Si-0.031Al-0.008N (wt pct.), was the subject of a recent study considering systematic variations of tensile properties with changes in austenite fraction and stability [14]. The steel was cold rolled, intercritically annealed in the ferrite-austenite region at 600 °C and 650 °C for 168 hr, and water quenched. These two temperatures were selected from the previous work to highlight material with displaying pronounced differences in austenite stability, initial yielding, work hardening behaviors [14] and transformation mechanism [3]. The long annealing cycle was used to provide sufficient time for diffusion to produce nearly equilibrium C and Mn concentrations in austenite and ferrite that stabilize austenite to room temperature on final cooling [3,14]. Tensile properties were measured using ASTM E-8 sub-sized samples with a 25.4 mm gauge length tested at a constant engineering strain rate of 5.74×10^{-4} s^{-1} continuously deformed to failure at room temperature [25].

In situ neutron diffraction, performed on the SMARTS diffractometer [26] at the Lujan Center at Los Alamos National Laboratory. Measurements of phase fractions, elastic lattice strains, and diffraction peak width were made during tensile deformation. SMARTS has two detector banks oriented at ±90° to the incident beam; one detector collects data for crystal orientations in the direction normal to the specimen thickness (*i.e.* in the transverse direction) and the second in the plane of maximum tension (*i.e.* in the axial direction), shown schematically in Figure 1 [26]. Tensile specimens for diffraction measurements were incrementally deformed: the actuator displacement paused, holding the sample at constant displacement, and diffraction

patterns were recorded. Applied stresses for the *in situ* diffraction data presented here are engineering stress on the sample at the end of the hold for neutron diffraction measurement.

Four phases were identified during the analysis of the diffraction data: thermodynamically stable body centered cubic (BCC) ferrite (α), metastable face centered cubic (FCC) austenite (γ), hexagonal close packed (HCP) epsilon (ε) martensite, and body centered tetragonal (BCT) alpha prime (α') martensite. Representative indexed diffraction patterns from the axial diffraction direction are shown in Figure 2a and Figure 2b for the 600 °C and 650 °C annealed steels, respectively. Data from the as-annealed samples and after successive increments of tensile strain are shown in Figure 2. Note, the diffraction peak corresponding to the ε martensite $\varepsilon_{\{101\}}$ planes was mislabeled previously [14] and is correctly indexed here. As the sample was deformed, metastable austenite transformed to ε-martensite and α'-martensite and the phase fractions of these constituents varied with strain. Whole pattern Rietveld analysis, performed with the GSAS software package, was employed to determine the austenite fraction at each strain increment using data from both diffraction directions [27,28]. The amount of ε martensite was calculated using only data collected from the axial diffraction direction, as ε martensite was not quantifiable in the transverse diffraction data. The amount of α' martensite was estimated by subtracting the sum of the amounts of austenite and ε martensite (measured with neutron diffraction) and the predicted intercritical ferrite amount (estimated with ThermoCalc software [29]) from the whole.

Single peak fitting using the Rawplot subroutine of GSAS was performed to measure the interplanar spacing as a function of applied stress and served to highlight representative orientation dependent lattice strains. A Gaussian function was fit to select peaks for each phase to determine the interplanar spacing and peak width at each increment of deformation. Elastic

lattice strains for each set of diffraction planes (ε_{hkl}) were calculated using Eq. 1.

(1) $\varepsilon_{hkl} = (d^{\sigma}_{hkl} - d^{0}_{hkl})/d^{0}_{hkl}$

d^{σ}_{hkl} is the *{hkl}* interplanar spacing averaged over a set of grains with *{hkl}* plane normals parallel to the diffraction vector measured at an incremental applied stress, and d^{0}_{hkl} is the interplanar spacing in the 'stress-free' condition. Stress relaxation during the pause in actuator displacement for the diffraction measurement likely produced a slight redistribution of the elastic stresses between phases resulting in small changes in the amount of plastic strain, which were ignored in the present case. Ferrite and austenite 'stress-free' interplanar spacings were determined by extrapolating the linear portion of the true stress-lattice strain curve below macroscopic yield point to zero load to remove the effects of sample and fixture unbending at low stresses. Calculation of lattice strains based on the initial unloaded lattice parameter allows for accurate representation of lattice strains that develop with deformation; however, initial residual stresses that may have formed during processing are not captured [22,30].

The BCC ferrite and BCT α' martensite phases were indexed as the same BCC structure for the 600 °C annealed steel as no tetragonality was resolvable in the diffraction data. Tetragonality was readily observable in fresh α' martensite in the 650 °C annealed steel in the axial direction at stresses above the yield stress; the $\alpha'_{\{200/002\}}$ and $\alpha'_{\{211/112\}}$ doublets were analyzed using single peak fitting. α' martensite lattice strains in the 650 °C annealed steel at high stress were extrapolated back to zero load, the residual strain at zero load was small, and it was therefore assumed that α' followed a constant slope stress-lattice strain path with loading.

The hexagonal close packed (HCP) ε martensite $\varepsilon_{\{101\}}$ peak was observed in the 650 °C annealed steel as heat treated, and developed during deformation of both steels. Lattice strains

for ε martensite in the 650 °C annealed steel were calculated using the same methodology as ferrite and austenite since ε martensite was always resolvable in the diffraction data. For the 600 °C annealed steel, ε martensite appeared after the initiation of plastic flow, lattice strains for this condition were calculated from the first appearance of ε-martensite and were offset using the yield plateau stress and a calculated $\varepsilon_{\{101\}}$ elastic modulus of 314 GPa [31,32].

Peak widths were also determined using single peak fitting. Instrumental peak broadening was assumed to be constant and represented in the peak widths at zero load and was removed from each subsequent measurement using Eq. 2

(2) $$B_{hkl} = (B^{\sigma}_{hkl}{}^2 - B^{0}_{hkl}{}^2)^{0.5}$$

where B^{σ}_{hkl} is the peak width at some applied stress, B^{0}_{hkl} is the unloaded peak width, and B_{hkl} is the instrument adjusted peak width, allowing changes in peak width with deformation to be monitored. Relative changes in peak width may be used as a qualitative indicator of either dislocation density changes or changes in crystallite size with plastic deformation of the constituent phases [33]. Changes in peak width due to plastic strain and dislocations are inversely dependent on interplanar spacing while crystallite size effects are independent of interplanar spacing.

3.0 RESULTS

3.1 TENSILE PROPERTIES

Figure 3a presents quasi-static engineering tensile stress-strain curves for samples of the 7.1-Mn steel annealed at 600 °C and 650 °C and continuously deformed to failure at room temperature [25]. Figure 3a also includes data recorded during *in situ* neutron diffraction. During *in situ* testing the sample deformation was paused for the neutron diffraction measurements; a small amount of stress relaxation during the time required for the diffraction measurement was

observed and is manifested by the load drops observed in Figure 3a. Slightly higher strengths were recorded during *in situ* testing, an approximately 50 MPa offset, and are attributed to room temperature ageing of the samples during the time between quasi-static and neutron diffraction testing [34]. After holding for the diffraction measurements a return of the yield point was observed, particularly for the steel intercritically annealed at 600 °C, indicating some degree of static strain ageing during the test.

Tensile properties were dependent on annealing temperature and ranged from low yield strength and high ultimate tensile strength (260 MPa and 1200 MPa, respectively, in the quasi-static tested sample) with limited total elongation (10 pct.) for the 650 °C annealed steel, to high ultimate tensile strength (870 MPa) and total elongation (41.5 pct.) for the 600 °C annealed steel. Discontinuous yielding and a distinct Lüders plateau were present in the 600 °C annealed steel. In contrast, a pronounced inflection in the stress strain behavior occurred during yielding in the steel annealed at 650 °C. The gray bands in the Figure 3a shows the stresses for these distinct yielding behaviors. Figure 3b highlights the instantaneous work hardening rate for the two steels as a function of applied true stress. A region of positive slope in the work hardening curve was present in both conditions after yielding and was related to austenite to martensite transformation [14].

3.2 Evolution of Austenite Volume Fraction

Figure 4 shows the dependence of the weight fraction of austenite, α', and ε martensite on the applied stress. The as-heat-treated steels consisted predominantly of a mixture of equiaxed recrystallized ultra fine austenite and ferrite grains with a grain size in the range of 0.9 μm to 1.5 μm; detailed descriptions of the microstructures may be found elsewhere [3,14]. Annealing at 600 °C resulted in 39 wt pct. austenite at room temperature in a ultra fine ferrite matrix. The

650 °C annealed steel retained 47 wt pct. austenite with approximately 1 wt pct. ε martensite and 15 wt pct. α' martensite forming *via* athermal transformation in the austenite on cooling from the annealing temperature. The austenite fractions presented here differ slightly (from 43.5 wt pct to 47.2 wt pct in the 650°C annealed steel and from 33.3 wt pct. to 38.8 wt pct. in the 600 °C annealed steel) from previously published values [14] due to the inclusion of the negative scattering length for the interaction of Mn with neutrons, not considered in earlier data analysis procedures. In addition to the overall transformation rates as determined by whole pattern Rietveld fitting, relative changes in the diffracted intensity of individual peaks are related to the amount of transformation for groups of similarly oriented grains. To highlight changes in orientation specific transformation, the diffracted peak intensity from the individual austenite $\gamma_{\{220\}}$ and $\gamma_{\{311\}}$ planes are plotted as a function of applied stress in Figure 5 for both annealing conditions.

As shown in Figure 4 the amount of ε and α' martensite in the 650 °C annealed steel increased rapidly with increasing applied stress immediately after yielding and during the period of high initial work hardening. The amount of ε martensite in the steel increased to twice the initial value at approximately 450 MPa. The fraction of martensite in the steel continued to increase with increasing stress until 92 pct. of the initial austenite had transformed into α' or ε martensite. Austenite peak intensities for both the $\gamma_{\{220\}}$ and $\gamma_{\{311\}}$ planes decrease rapidly with applied stress and the data points essentially overlay, suggesting that the degree of austenite transformation was independent of grain orientation (Figure 5).

Neither α' nor ε martensite was present in the 600 °C annealed steel in the as heat treated condition; both appeared after the yield point elongation (Figure 4) [3]. The amount of ε martensite after discontinuous elongation was 2.5 wt pct. while formation of α' in this region

was negligible. After the yield point elongation, the weight fraction of ε martensite increased with deformation to a maximum of approximately 6 wt pct. at 800 MPa (Figure 4). Concurrent formation of α' with ε martensite was observed during continuous deformation and the weight fraction of α' martensite increased continually with increasing applied stress. Significant orientation dependence of transformation in the 600 °C annealed steel was observed (Figure 5) with the $\gamma_{\{220\}}$ planes decreasing in intensity more rapidly than the $\gamma_{\{311\}}$ planes.

3.3 Evolution of Diffraction Peak Width

Figure 6a and Figure 6b show relative changes in ferrite and austenite peak width for the 600 °C and 650 °C annealed steels, respectively. Figure 6a presents the ferrite $\alpha_{\{200\}}$ and $\alpha_{\{211\}}$ peak widths while Figure 6b shows the austenite $\gamma_{\{220\}}$ and $\gamma_{\{311\}}$ peak broadening. Ferrite peak widths in the 650 °C annealed steel increased rapidly immediately after yielding, at 330 MPa, but remained relatively constant with increasing applied stress between 450 MPa and approximately 700 MPa. Above 700 MPa the ferrite peak widths increased with increasing applied stress; the slope of the peak width as a function of plane index increased with increasing stress (*i.e.* the $\alpha_{\{200\}}$ peak becoming broader more rapidly than the $\alpha_{\{211\}}$ peaks). The austenite peaks also increased in width rapidly at yielding, similar to the ferrite data, and saturated above 450MPa. In contrast to the ferrite data however, the austenite peak widths did not increase significantly above 700MPa. The austenite $\gamma_{\{220\}}$ and $\gamma_{\{311\}}$ peak widths essentially overlay each other and no significant interplanar spacing dependence was observed.

In the steel annealed at 600 °C, the ferrite peak widths increased continuously after yielding; the austenite $\alpha_{\{200\}}$ peak (larger interplanar spacing) increased more rapidly than the $\alpha_{\{211\}}$ peak. Austenite peak widths increased monotonically after the initiation of plastic flow in the sample and showed significant plane index dependence and the $\gamma_{\{220\}}$ peak increased in width

much more rapidly that the $\gamma_{\{311\}}$ peaks. Recall that the axially oriented $\gamma_{\{220\}}$ also transformed to martensite more rapidly than the $\gamma_{\{311\}}$ oriented grains from the data in Figure 5.

3.4 LATTICE STRAIN RESULTS

Figure 7 shows the development of lattice strains as a function of applied stress for the 600 °C annealed steel in Figure 7a and Figure 7b and for the steel annealed at 650 °C in Figure 7c and Figure 7d. At least four unique data sets are presented in each figure, ferrite data for the $\alpha_{\{200\}}$ and $\alpha_{\{211\}}$ planes in the axial and transverse direction are plotted in Figure 7a and Figure 7c while the austenite data for the $\gamma_{\{220\}}$ and $\gamma_{\{311\}}$ planes in both sample directions are plotted in Figure 7b and Figure 7d. Figure 7c also includes data for martensite $\alpha'_{\{002\}}$ and $\alpha'_{\{112\}}$ planes as well as the $\varepsilon_{\{101\}}$ planes for the 650 °C annealed steel while Figure 7b includes data for the $\varepsilon_{\{101\}}$ planes after annealing at 600 °C. Figure 8 compares the $\alpha_{\{200\}}$ lattice strain data for both steels to emphasize changes in ferrite behavior with increasing applied stress. The observation of ε martensite in the selected steels allows unique insight into the austenite to martensite transformation with deformation due to the orientation relationship that exists between the phases [35,36]. As the transformation from austenite to ε martensite to α' martensite progressed, the $\gamma_{\{220\}}$, $\varepsilon_{\{101\}}$, and $\alpha'_{\{112\}}$ plane normals were parallel and the resulting lattice strain data can be used to make inferences about changes in the transformation [37,38].

Three distinct regions of deformation can be seen in the lattice strain data:

- In Stage 1, initial linear and reversible deformation of the sample was observed; in this region of deformation both constituents are loaded elastically. Lattice strains were tensile in the axial direction and compressive in the transverse direction for both ferrite and austenite, consistent with the Poisson effect.

- Stage 2 was signaled by abrupt lattice compression in austenite in both the axial and transverse directions during macroscopic yielding. With increasing stress a change in the slope of the ferrite lattice strain behavior was observed, while the strains in austenite were increasingly compressive.
- Stage 3 was characterized by the arrest in the increase of the lattice strain in ferrite in the axial direction.

Stress values corresponding to transition points between the deformation stages are labeled in each part of Figure 7 on the right side ordinate axes.

Stage 1 deformation was observed up to stresses near the Lüders plateau for the 600 °C annealed steel. Stage 2 deformation coincided with onset of macroscopic yielding at approximately 685 MPa for the steel annealed at 600 °C measured during *in situ* testing of the strain aged sample. During Stage 2 deformation the lattice strains for ferrite and austenite diverged with increasing applied stress. In both diffraction orientations a distinct negative offset, corresponding to lattice compression, occurred in austenite. The observed lattice strain divergence occurred clearly at the stress required for initiation of austenite transformation to martensite shown in Figure 4b. During Stage 2 deformation austenite developed increasingly compressive strains with increasing applied load, eventually resulting in essentially zero strain in the axial austenite planes at the end of austenite transformation. The development of compressive strains in the axial austenite lattice strain data was unexpected given the applied tensile load on the sample.

Stage 2 also initiated a change in slope in the lattice strain response in ferrite in the axial direction. In the 600 °C annealed steel a decrease in the slope with respect to the applied stress was observed, 75 GPa after yielding versus 170 GPa prior to yielding (Figure 8). In the

transverse orientation ferrite strains decreased in magnitude until essentially no elastic lattice strain was recorded (Figure 7a). Lattice strains in ferrite in the transverse direction remained essentially zero with increasing applied stress. Similar ferrite lattice strain behavior was recently reported by Blondé *et al.* [39] for a bainitic based TRIP steel deformed at or below room temperature. The lack of a transverse lattice strain in ferrite is likely a combination of physical compatibility constraints between constituents after the initiation of plastic flow, redistribution of stresses due to austenite transformation, and the decrease in transverse stress due to plastic deformation.

The third stage of deformation was characterized by a change in the slope of the ferrite lattice strains in the axial direction with respect to the applied stress at approximately 730 MPa in the 600 °C annealed steel. Ferrite lattice strains ceased to increase and remained essentially constant with increasing stress in Stage 3.

While the lattice strain data for the 650 °C steel show many parallels to the 600 °C steel, several key differences were apparent. First, Stage 2 deformation initiated around 330 MPa, near the 0.2 pct offset yield stress, and the abrupt compressive strains at the beginning of Stage 2 deformation were smaller in the 650 °C annealed steel (Figure 7d) compared to the 600 °C annealed steel (Figure 7b). Secondly, for the 650 °C annealed steel, the slope of the ferrite stress-lattice strain curve after initiation of plastic deformation increased from 170 GPa to 500 GPa for the $\alpha_{\{200\}}$ planes (Figure 8). In this deformation stage, ferrite in the 650 °C annealed steel was less stressed than during the initial elastic loading. Finally, the stress for the initiation of Stage 3 deformation was somewhat lower in the 650°C annealed steel than in the 600 °C annealed condition, approximately 700 MPa compared to 730 MPa (Figure 8).

ε martensite displayed two distinct behaviors after annealing at the selected temperatures. Annealing at 600 °C resulted in a similar lattice strain-applied stress path for the $\varepsilon_{\{101\}}$ and $\gamma_{\{220\}}$ lattice strains. In contrast, the lattice strain path for $\varepsilon_{\{101\}}$ planes in the 650 °C annealed steel followed the $\alpha'_{\{112\}}$ planes.

4.0 DISCUSSION

4.1 AUSTENITE TRANSFORMATION MECHANISM

A complementary transmission electron microscopy (TEM) study on the two steels discussed here indicated that austenite in the 650 °C steel transformed *via* stress-induced transformation, due to the relatively low Mn-enrichment in austenite and correspondingly low stability against transformation, while strain-assisted mechanisms dominated transformation in the 600 °C annealed steel as a result of the mechanical stability of austenite afforded by the high C and Mn level in austenite after annealing at 600 °C [3].

The *in situ* diffraction data presented provide a unique perspective to verify the TEM results and highlight changes in the austenite-to-martensite transformation mechanism. In the 650 °C annealed steel, the austenite peak widths were essentially constant with deformation above 450 MPa (Figure 6b), suggesting limited plastic deformation in austenite. Additionally, the observation of the α' martensite *c*-axis is strong evidence that Zener ordering of supersaturated C to octahedral lattice sites during stress-induced transformation was preferred compared to Snoek ordering of C atoms to dislocations in plastically deformed austenite. These two observations, combined with the rapid rate of initial transformation at stresses below the expected yield strength for either UFG ferrite or austenite, are clear indicators that austenite in the 650 °C annealed steel transformed initially *via* stress-induced martensite mechanisms on preexisting nucleation sites. In the 600 °C annealed steel, austenite peak widths increased at stresses above the stress required for austenite transformation, which indicates significant plastic

deformation in austenite by dislocation slip. Additionally, there was no observable α' martensite *c*-axis in the 600 °C annealed steel, indicating interstitial C atoms moved to dislocations *via* rapid Snoek ordering [40,41] rather than Zener ordering. In this case austenite transformation was *via* strain-assisted martensite on ε martensite nucleation sites formed during plastic deformation of austenite [3].

The change in ε martensite behavior mirrors the change in austenite transformation mechanisms from strain-assisted to stress-induced for the 600 °C and 650 °C annealed steels, respectively. The relatively low stability of austenite in the 650 °C annealed steel resulted in multiple crystallographic variants of thin plate ε martensite and α' laths formed during athermal transformation on quenching [3]. As a transition phase that formed during athermal transformation, ε martensite that was present after quenching was adjacent to athermal α' martensite, and was constrained by neighboring α' martensite rather than austenite. The $\varepsilon_{\{101\}}$ and $\alpha'_{\{112\}}$ planes, which were oriented parallel to each other through transformation, display a similar lattice strain-applied stress response because of the interfacial constraint (Figure 7c). As the hard α' martensite accepted an increasing fraction of the applied stress with increasing austenite transformation the thin plates of ε martensite were similarly pulled in tension.

The stress during Lüders deformation in the 600 °C annealed steel was essentially the same as the stress for the onset of Stage 3 deformation in the 650 °C annealed steel (Figure 8) suggesting that bulk yielding after annealing at the lower temperature was controlled by the strain aged ferrite matrix. Austenite deformation during Lüders elongation was likely limited to accommodation of the ferrite yielding strain. Peak broadening in austenite was due to the separation of partial dislocations and the formation of thin ε martensite plates on austenite stacking fault intersections [3]. The formation of ε martensite on dislocation structure resulted in

some of the $\gamma_{\{220\}}$ planes being replaced by the parallel equivalent $\varepsilon_{\{101\}}$ planes during Lüders deformation, shown by the decrease in the $\gamma_{\{220\}}$ peak intensity during Lüders deformation in Figure 5. The formation of ε martensite on strain induced austenite deformation structure resulted in ε martensite only being present in the axial diffraction data due to the orientation dependence of the maximum applied shear stress during tensile deformation and selection of dislocation slip only on suitably aligned austenite grains. The presence of textured ε martensite is therefore an indicator of dislocation slip in austenite and strain assisted martensite transformation [35,36] Due to the replacement of only specific austenite lattice planes by ε martensite, the lattice strain-applied load path of the $\varepsilon_{\{101\}}$ planes continued the loading path of the $\gamma_{\{220\}}$ planes in subsequent deformation.

4.2 Interpretation of Austenite Lattice Strains

In addition to producing the changes in macroscopic yielding and work hardening behavior between the two steels, the changes in relative austenite stability between the 7.1-Mn steel annealed at 600 °C and 650 °C resulted in pronounced changes in the distribution of internal lattice strains with deformation. The gradual reduction of lattice strains in austenite in the axial direction (Figure 7b and Figure 7d) could be explained by the decrease in austenite fraction decreasing the effective load on austenite due to the formation of martensite. However, this mechanism would not account for the continual decreases in the transverse austenite lattice strains with increasing austenite transformation and deformation.

The decrease in austenite lattice strains at the onset of plastic deformation was instead due to the internal stresses caused by martensite formation, the associated average volume expansion of transformation, and the effect of the local strength increase by the formation of C-saturated martensite. The development of internal stresses due to the volume expansion of

transformation may be considered by developing a simple framework to impose the change in volume between constituents with transformation on the apparent lattice strains. During deformation, a selected volume in an austenite grain transforms to martensite with an associated net increase in the volume of the transformed region. As the surrounding austenite constrains the volume expansion, internal stresses due to the constraint develop in both phases. Austenite may deform plastically to accommodate the transformation [21] and is also subjected to a state of compression around the transformed volume. Martensite is also hydrostatically compressed by constraint of the volume expansion. Austenite plastic deformation in response to the volume expansion of transformation would reduce the compressive stresses in both austenite and martensite. The resolved elastic hydrostatic stresses resulting from constraint of the transformation appear in the diffraction data as compressive elastic lattice strains. Since an austenite grain is initially large compared to a martensite lath, it is likely that only austenite within an individual grain or adjacent to freshly transformed martensite is strained.

A simple framework may be considered, applying the Bain correspondence between atom sites during transformation from austenite to martensite, to interpret the observed lattice strain data incorporating the effect of austenite transformation during deformation [17]. To represent the lattice strains, the total elastic strain in austenite is assumed to be the sum of the linear elastic response to applied tensile load and the elastic internal stresses resulting from constraint of the volume change of austenite transformation to martensite. The relative magnitude of the average volume strain can be estimated by calculating the martensite and austenite lattice parameters using empirical expressions and the ThermoCalc software predictions for austenite C and Mn content from Table 1. The estimated and measured phase lattice parameters for austenite and martensite and ferrite are presented in Table 2.

The volume strain (ε_V) was calculated by taking the average change in lattice parameter and assuming the transformation followed the Bain lattice correspondence using Eq. 3.

(3) $\varepsilon_V = 1/3\ (\varepsilon_1 + \varepsilon_2 + \varepsilon_3) = 1/3\ (2\varepsilon_{1,2} + \varepsilon_3)$

Estimated lattice strains for the two annealing temperatures are included in Table 3 [29,42–47]. The calculated volume strain (ε_V) is assumed to represent an effective average linear strain imposed by the transformation on the lattice neglecting the rigid body rotation contribution of the transformation. The values of ε_V were estimated to be 0.0191 and 0.0196 for the 600 °C and 650 °C annealed conditions respectively (Table 3). The difference in volume strain between the two annealing temperatures is due to differences in the austenite C and Mn contents predicted by ThermoCalc software [14].

The lattice strains resulting from transformation are assumed to dominate the load partitioning normally observed in multi-phase microstructures at the onset of plastic deformation. The bulk material is considered an isotropic ideal two-phase mixture, neglecting initial crystallographic texture or variations in austenite morphology. The linear contribution to the lattice strain from austenite transformation is assumed to be the product of $f_{\alpha'}$, the amount of martensite formed during deformation calculated from the data in Figure 4, and the average volume strain of the transformation from Table 3. Internal lattice strains in the axial direction for austenite (ε_γ) may be represented by:

(4) $\varepsilon_\gamma = \sigma/E_\gamma - (f_{\alpha'})\varepsilon_V$

where σ is the applied tensile stress, and E_γ is bulk the Young's modulus for austenite. Since a bulk modulus is used in Eq. 4 the model predictions represent an averaged constraint effect of the transformation volume strain by austenite. Plots of the observed phase strains from single

peak fits for the austenite $\gamma_{\{220\}}$ and $\gamma_{\{311\}}$ reflections in the axial diffraction orientation compared to the predictions for ε_γ from Eq. 4 assuming axial loading for the 600 °C and 650 °C annealed steels are presented in Figure 9. While the interpretive model is not a rigerous representation of the real microstructural constraint of the tranformation of austentie to martensite, it allows discussion of the unexpected decrease in the lattice strains observed for austenite.

For the 600 °C annealed steel, austenite lattice strains in both directions are reasonably represented with a maximum strain separation of 0.011 between the model and data (Figure 9). The slope of the interpretive line for austenite at higher stresses, *i.e.* above 675 MPa, agrees well with the trend shown in the experimental data for both diffraction directions. The good agreement between the interpretive model and the observed data indicate that constraint of the volume expansion of transformation is the cause of the abrupt decrease in austenite lattice strains during plastic deformation.

Comparisons between the interpretive model and the data for the 650 °C annealed steel are less successful. The dashed red line in Figure 9 was calculated using the estimated volume strain of 0.0196, comparing these predictions to the observed data for the 650 °C annealed steel shows that the austenite lattice strains become negative at the onset of austenite transformation and the estimated lattice strains decrease much too rapidly for an increase in applied stress (and thereby fraction transformed). The effect of the volume expansion of austenite on the austenite lattice strain does not appear to meet the criteria of the interpretive model from Eq.4 for the 650 °C annealed steel. However, reducing the apparent volume strain to the linear transformation strain in one direction (*i.e.* $(1/3)\varepsilon_V$) produced the solid red line in Figure 9. Reducing the magnitude of the transformation strain resulted in the interpretive model representing the

observed trend in lattice strain data, and two factors are suggested as to why there is the apparent change in the contribution of the volume change of transformation to the lattice strain data.

First, a significant amount of athermal martensite subdivided the initial austenite pools in the as heat treated steel after annealing at 650 °C [3]. Additionally, Figure 4 shows that further martensite formation was very rapid for increasing applied stresses between yielding and approximately 450 MPa. Constraint of the volume expansion of transformation by athermal α' martensite rather than austenite may occur in the 650 °C annealed steel due to the reduction in austenite pool size resulting from subdivision by hard α' martensite (evidenced by the grain size change indicated by the lattice plane index independent peak broadening in Figure 6b). As the relative distance between martensite laths decreased, α' martensite rather than the remaining austenite would constrain the volume expansion of any additional transformation, the lattice strain decrease therefore would not appear in the austenite diffraction data.

The second factor contributing to the reduction in volume strain is the change in austenite transformation mechanism. In the 650 °C annealed steel austenite transformation was on existing nucleation sites and occurred due to increasing driving force supplied by the applied stress. Nucleation on existing sites is dominated by the shear component of transformation rather than the Bain correspondence utilized in the simple interpretive model [48]. Changes in the crystallographic orientation of the volume expansion and constraint of the transformation due to the shear component of the transformation may reduce the apparent compression in the lattice strain with austenite transformation [49,50]. In the 600 °C annealed steel transformation occurred on nucleation sites formed by plastic deformation in austenite. Nucleation on sites oriented for plastic flow likely precludes selection of crystal variants specifically to minimize volume strain,

allowing reasonable agreement between the interpretative model and the data in Figure 9 for the 600 °C annealed steel.

4.3 YIELDING SEQUENCE AND WORK HARDENING

As discussed above, austenite lattice strains were dominated by constraint of austenite transformation. However, interpretation of the austenite lattice strains in isolation does not explain the work hardening behavior observed in Figure 3. In particular, the coupled analysis of the lattice strain and peak broadening data for all four observed phases, combined with the overall austenite transformation kinetics, highlight the complex deformation sequence between constituents in fine-grained duplex TRIP steels.

Annealing at 650 °C resulted in a low yield strength, high ultimate tensile strength and relatively low total elongation. Yielding in the 650 °C annealed steel was *via* rapid stress induced transformation of austenite to martensite; during yielding the stress in austenite was limited by the transformation criteria. The inflection in the sample stress-strain behavior seen in Figure 3a was produced by increasing stresses in ferrite and martensite recorded by the lattice strains shown in Figure 7c and Figure 7d. After the initial inflection in the yielding behavior an increase in the slope of the ferrite lattice strains between Stage 1 and Stage 2 was observed (Figure 8). The increase in ferrite slope was a result of the rapid replacement of austenite by a much harder phase, *i.e.* martensite, during Stage 2 deformation reducing the relative fraction of the sample stress applied to ferrite. Increases in ferrite peak width during Stage 2 deformation were minimal, indicating limited ferrite plastic deformation by dislocation slip. With increasing applied stress α' and ε martensite were loaded elastically and accepted an increasing fraction of the applied load. The dynamic replacement of austenite by martensite with associated composite strengthening

produced the high work hardening rate during Stage 2 deformation (between 400 and 650 MPa) in Figure 3b.

Eventually austenite replacement by martensite increased the strength of the steel to the point where extensive ferrite plastic deformation occurred, thereby initiating Stage 3 deformation at approximately 700 MPa. During Stage 3 deformation ferrite lattice strains saturated and remained essentially constant with increasing stress (Figure 7c). Austenite transformation was exhausted at stress levels for Stage 3 deformation and the steel behaved as a high martensite fraction dual-phase steel [14,51]. The stress-lattice strain line for α' martensite remained consistent during both Stage 2 and Stage 3 deformation, indicating that the stress in martensite increased at a constant rate for increasing sample stress throughout the range of tested stresses. Dislocation multiplication and work hardening by ferrite dominated the plastic strengthening during Stage 3 deformation. The neutron diffraction data, therefore, clearly indicate a piecewise deformation sequence in the 650 °C annealed steel whereby plastic deformation was dominated by austenite transformation at low stresses transitioning to a regime determined by ferrite plastic flow at high stresses. While the sequential determination of deformation by individual phases produced continuous yielding and a high ultimate tensile stress, the rapid depletion of austenite at yielding resulted in relatively low hardening rates at high stresses and rapid plastic instability.

Comparing the diffraction peak broadening, austenite transformation rate, and lattice strain data between the 600 °C and 650 °C annealed steels highlights several significant mechanistic differences between the two conditions resulting in the observed change in tensile properties. The width of both ferrite and austenite diffraction peaks increased during yield point elongation and initial deformation of the steel annealed at 600 °C (Figure 6a and Figure 6b). After Lüders deformation, during Stage 2 deformation, both ferrite and austenite peak widths

continued to increase and the relative rate of change in peak width was dependent on interplanar spacing, suggesting that both phases deformed plastically. During Stage 2 deformation each microstructural constituent contributed to strengthening: α' martensite accepted load as it formed; ferrite work hardened during plastic deformation, however at a relatively low rate due to stress partitioning to deformation-induced martensite, as evidenced by the increases in peak widths; and austenite deformed plastically in addition to transforming to martensite. The observed decrease in ferrite slope during Stage 2 deformation compared to Stage 1 deformation (Figure 8) was likely the result of the presence of an increasing volume fraction of martensite. In the 600 °C annealed steel, rapid Snoek ordering of carbon atoms to dislocations relaxed the *c*-axis distortion of the α' martensite [40,41] causing overlap with the ferrite diffraction peaks and an observed pseudo strain. α' martensite will carry a progressively higher fraction of the total applied sample stress as it forms with increasing sample strain, resulting in an increase in the composite ferrite-α' martensite lattice strain. As the rate of austenite transformation decreased, and Stage 3 deformation initiated, the slope of the ferrite lattice strains increased. The arrest in ferrite lattice strains shown in Figure 8 and the peak broadening data in Figure 6a indicate that ferrite plastic deformation dominated deformation of the steel above this point.

Shared plastic deformation of both ferrite and austenite in the 600 °C annealed steel, combined with the relatively high chemical stability of austenite against transformation provided by the high C and Mn content in austenite, resulted in sustained work hardening to high sample stresses and strains. The sustained work hardening behavior observed for the 600 °C annealed steel in Figure 3b, resulting from shared deformation between multiple phases, was is in stark contrast to the to the rapid in initial work hardening rate observed in the 650 °C annealed steel resulting from segregated deformation between constituents. Design of microstructures for

AHSS development should therefore consider not only the stabilization of austenite to room temperature but also the relative flow stresses of the various constituent with regard to the austenite transformation criteria in order to maximize both strength and ductility in the steel.

5.0 CONCLUSIONS

In situ neutron diffraction was used to measure phase-specific lattice strains, peak broadening, and phase fraction in a 7.1-Mn 0.1-C TRIP steel annealed at 600 °C and 650 °C for 168 hr. These data were used to determine the progression of yielding and plastic deformation between constituent phases in each of the steels with sample deformation. Three regimes of deformation were identified; the stress loci between these stages are related to relative austenite stability. Several key conclusions may be drawn for each of the conditions addressed here:

- Yielding in the 650 °C annealed steel was dominated by stress-induced austenite transformation to martensite, resulting in high initial work hardening rate. However, as the austenite transformation was very rapid and concluded before ferrite plastic deformation could begin and the work hardening rate decreased rapidly at high strains. The progression from austenite to ferrite-dominated deformation resulted in a high ultimate tensile strength and a relatively low ductility despite the very high initial work hardening rate.
- Yielding in the 600 °C annealed steel was controlled by localized plastic deformation of strain-aged recrystallized ferrite. After the initial yield point elongation, homogenous plastic deformation and austenite transformation were initiated; both ferrite and austenite plastically deformed during this stage. The gradual transformation of austenite to martensite resulted in a sustained work hardening plateau, producing high strength and ductility irrespective of the relatively low work hardening rate at a given stress compared to the 650 °C annealed steel.

These results highlight the complex interactions between microstructural constituents in high austenite fraction steels anticipated for the third generation AHSS. Design of steels to meet

the evolving requirements for automotive design should focus on microstructures that display sustained austenite transformation to avoid plastic flow localization and maintain work hardening with deformation, in a high strength matrix with some amount of useful plasticity.

6.0 ACKNOWLEDGEMENTS

The authors gratefully acknowledge the support of the National Science Foundation for support under award CMMI-0729114 and the sponsors of the Advanced Steel Processing and Products Research Center, an industry/university cooperative research center at the Colorado School of Mines. This work also benefited from use of the Lujan Neutron Scattering Center at LANSCE, which is funded by the Office of Basic Energy Sciences (DOE). Los Alamos National Laboratory is operated by Los Alamos National Security LLC under DOE Contract DE AC5206NA25396. Additionally the authors would like to thank U. S. Steel for providing the experimental material, T.A. Sisneros at the Lujan Center for his assistance with the neutron experiments, Professors J.G. Speer and C.J. Van Tyne at the Colorado School of Mines for helpful discussions surrounding the manuscript.

The material in this article is intended for general information only. Any use of this material in relation to any specific application should be based on independent examination and verification of its unrestricted availability for such use and determination of suitability for the application by professionally qualified personnel. No license under any patents or other proprietary interest is implied by the publication of this article. Those making use of or relying upon the material assume all risks and liability arising from such use or reliance.

7.0 REFERENCES

[1] Int. Iron Steel Institute, Comm. Automot. Appl. (n.d.).
[2] E. De Moor, P.J. Gibbs, J.G. Speer, D.K. Matlock, J.G. Schroth, AIST Trans. 7 (2010) 133.
[3] B.C. De Cooman, P.J. Gibbs, S. Lee, D.K. Matlock, Metall. Mater. Trans. A 44A (2013) 2563.
[4] S. Lee, S.-J. Lee, B.C. De Cooman, Scr. Mater. 65 (2011) 225.
[5] R.L. Miller, Metall. Trans. 3 (1972) 905.
[6] M.J. Merwin, Mater. Sci. Forum 539-543 (2007) 4327.
[7] M.J. Merwin, Steel Res. 2007-01-03 (2007).
[8] M.J. Merwin, Mater. Sci. Technol. 5 (2007) 515.
[9] H. Huang, O. Matsumura, T. Furukawa, Mater. Sci. Technol. 10 (1994) 621.
[10] D. Suh, S.-J. Park, T.-H. Lee, C. Oh, S. Kim, Metall. Mater. Trans. A 41 (2009) 397.
[11] S.J. Kim, Mater. Sci. Forum 638-642 (2010) 3313.
[12] S. Lee, K.Y. Lee, B.C. De Cooman, Mater. Sci. Forum 654-656 (2010) 286.
[13] S. Lee, S.-J. Lee, S.S. Kumar, K. Lee, B.C. De Cooman, Metall. Mater. Trans. A 42 (2011) 3638.
[14] P.J. Gibbs, E. De Moor, M.J. Merwin, B. Clausen, J.G. Speer, D.K. Matlock, Metall. Mater. Trans. A 42 (2011) 3691.
[15] S. Harjo, Y. Tomota, P. Lukas, D. Neov, M. Vrana, P. Mikula, M. Ono, Acta Mater. 49 (2001) 2471.
[16] T. Han, P. Dawson, Mater. Sci. Eng. A 405 (2005) 18.
[17] E.C. Bain, Trans. AIME 70 (1924) 25.
[18] J.R. Patel, M. Cohen, Acta Metall. 1 (1953) 531.
[19] Y. Tomota, H. Tokuda, Y. Adachi, M. Wakita, N. Minakawa, a. Moriai, Y. Morii, Acta Mater. 52 (2004) 5737.
[20] P.J. Jacques, Q. Furnemont, S. Godet, T. Pardoen, K.T. Conlon, F. Delannay, Philos. Mag. 86 (2006) 2371.
[21] P.J. Jacques, Q. Furnemont, F. Lani, T. Pardoen, F. Delannay, Acta Mater. 55 (2007) 3681.
[22] O. Muransky, P. Sittner, J. Zrnik, E.C. Oliver, J. Zrnı, Acta Mater. 56 (2008) 3367.
[23] A.M. Streicher-Clarke, J.G. Speer, D.K. Matlock, B.C. De Cooman, D. Williamson, Metall. Mater. Trans. A Mater. Trans. A 36 (2005) 907.
[24] K. Asoo, Y. Tomota, S. Harjo, Y. Okitsu, ISIJ Int. 51 (2011) 145.
[25] in:, 2008 Annu. B. Stand. Vol. 03.01 Met. - Mech. Test. Elev. Low Temp. Test. Metallogr., ASTM, 2008, pp. 64–88.
[26] M.A.M. Bourke, D.C. Dunand, E. Ustundag, Appl. Phys. A Mater. Sci. Process. 74 (2002) s1707.
[27] H. Rietveld, J. Appl. Crystallogr. 2 (1969) 65.
[28] A. Larsen, R.B. Von Dreele, (1986) LAUR 86.
[29] B. Lee, B. Sundman, (1999).
[30] T. Ungár, Scr. Mater. 51 (2004) 777.
[31] T.S. Hutchison, D.C. Baird, The Physics of Engineering Solids, 2nd ed., John Wiley and Sons, New York, NY, 1968.
[32] S. Merkel, J. Shu, P. Gilley, H. Mao, R. Hemley, J. Geophys. Res. 110 (2005) 1.
[33] A.R. Stokes, A.J.C. Wilson, Mathmatical Proc. Cambridge Philos. Soc. 40 (1944) 197.
[34] H.E. Rosinger, G.B. Craig, W.J. Bratina, Mater. Sci. Eng. 5 (1970) 163.
[35] F. Lecroisey, A. Pineau, Metall. Trans. 3 (1972) 387.
[36] G.B. Olson, M. Cohen, Metall. Trans. A 6 (1975) 791.
[37] H. Schumann, Krist. Und Tech. 9 (1974) 1141.
[38] E. Gartstein, A. Rabinkin, Acta Metall. 27 (1979) 1053.
[39] R. Blondé, E. Jimenez-melero, L. Zhao, J.P.P. Wright, E. Brück, S. van der Zwaag, N.H. van Dijk, E. Bru, S. Van Der Zwaag, N.H. Van Dijk, Acta Mater. 60 (2012) 565.
[40] L.I.U. Cheng, N.M. Van Der Pers, A. Bottger, T.H. De Keijser, 22 (1991).
[41] K. Ullakko, V.G. Gavriljuk, V.M. Nadutov, Metall. Mater. Trans. A 25 (1994) 889.
[42] S.-J. Lee, S. Lee, B.C. De Cooman, Scr. Mater. 64 (2011) 649.
[43] S.-J. Lee, M. Lusk, Y. Lee, Acta Mater. 55 (2007) 875.
[44] N.N. Lipchin, N.L. Olson, S.A. Kokovyakina, Met. Sci. Heat Treat. 14 (1972) 7.
[45] C. Li, F. Sommer, E. Mittemeijer, Mater. Sci. Eng. A 325 (2002) 307.
[46] S. Lee, Y. Lee, Scr. Mater. 52 (2005) 973.
[47] Thermo-Calc Software, Stockholm, Sweden, (2009).

[48] G.B. Olson, Metall. Mater. Trans. A 13 (1982) 1907.
[49] C. Magee, Transformation Kinetics, Microplasticity and Ageing of Marteniste in Fe-3Ni, Carnegie Institute of Technologie University, 1966.
[50] H.K. Yeddu, A. Borgenstam, J. Ågren, Acta Mater. 61 (2013) 2595.
[51] L.F. Ramos, D.K. Matlock, Metall. Mater. Trans. A 10 (1979) 259.

8.0 LIST OF TABLES

Table 1 – Predicted Intercritical Austenite Composition

Table 2 – Measured and Estimated Lattice Parameters for Ferrite and Austenite [[42–46][47][29]]

Table 3 – Estimated Lattice Strains for Austenite to Martensite Transformation [[42–46] [47][29]]

9.0 LIST OF FIGURES AND FIGURE CAPTIONS

Figure 1 Schematic of the SMARTS diffractometer highlighting the orientation of planes diffracting in the axial and transverse orientations [26].

Figure 2 Representative *in situ* neutron diffraction patterns during uniaxial tensile deformation for a) 600 °C and b) 650 °C for 168 hr. Peak indices are indicated on the bottom of the figure. Engineering stresses from the end of each diffraction measurement are indicated on the right side of the figures. Intensity plotted in arbitrary units (AU).

Figure 3 a) Room temperature tensile engineering stress strain curves for both quasi-static and interrupted neutron *in situ* neutron diffraction samples. Open symbols on the in situ curves correspond to strains for diffraction pattern measurements. b) Instantaneous true work hardening rate ($d\sigma/d\varepsilon$) for the room temperature tested tensile samples. Plotted instability criteria corresponds to the instantaneous work hardening rate equaling the true stress on the sample. Quasi-static tensile tests used a constant engineering strain rate of 5.47×10^{-4} s^{-1} on ASTM E-8 geometry with a 25 mm gauge length.

Figure 4 Development of relative austenite, ε, and α' martensite amounts as a function of applied stress for 7.1-Mn steel annealed 168 hr. at the temperatures indicated on the figures. Austenite and ε martensite fractions measured with *in situ* neutron diffraction, α' fraction estimated by subtracting the measured austenite, ε, and intercritical ferrite amounts from 100 pct

Figure 5 Relative austenite peak intensities for austenite $\gamma_{\{220\}}$ and $\gamma_{\{311\}}$ planes for 600 °C and 650 °C annealed steels with respect to the applied tensile stress in the axial direction as determined by single peak fitting of *in situ* neutron diffraction data

Figure 6 Instrument corrected peak width for 600 and 650 °C annealed steels with respect to the applied tensile stress in the axial direction as determined by single peak fitting of *in situ* neutron diffraction data for a) ferrite $\alpha_{\{200\}}$ and $\alpha_{\{211\}}$ peaks and b) austenite $\gamma_{\{220\}}$ and $\gamma_{\{311\}}$ peaks

Figure 7 Elastic phase strains for the 7.1-Mn steel annealed at 600 °C for a) ferrite and b) ε martensite and austenite and data from the 650 °C annealed steel for c) ferrite, ε and α' martensite and b) austenite. In each figure lattice strain data for both the axial and transverse directions are plotted with respect to macroscopic tensile stress for 600 °C annealed steel

Figure 8 Ferrite $\alpha_{\{200\}}$ lattice strain behavior in the axial diffraction direction as calculated using single peak fitting for the 600 °C and 650 °C annealed steel. Data are replotted from Figure 7a and Figure 7c for clarity

Figure 9 Interpretive model (lines) and observed (points) $\gamma_{\{311\}}$ lattice strains in the axial direction for austenite for the 600 °C and 650 °C annealed steels in the axial and transverse directions. Model calculated using volume strain of $19.1*10^{-3}$ and $7.5*10^{-3}$ for the 600 °C and 650 °C annealed steels, respectively

11.0 FIGURES

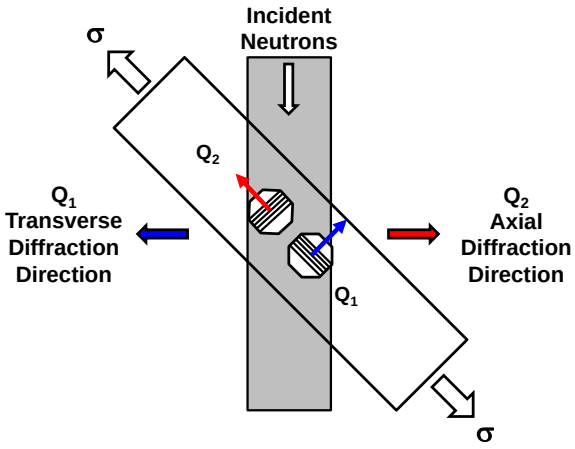

Figure 1 Schematic of the SMARTS diffractometer highlighting the orientation of planes diffracting in the axial and transverse orientations [26].

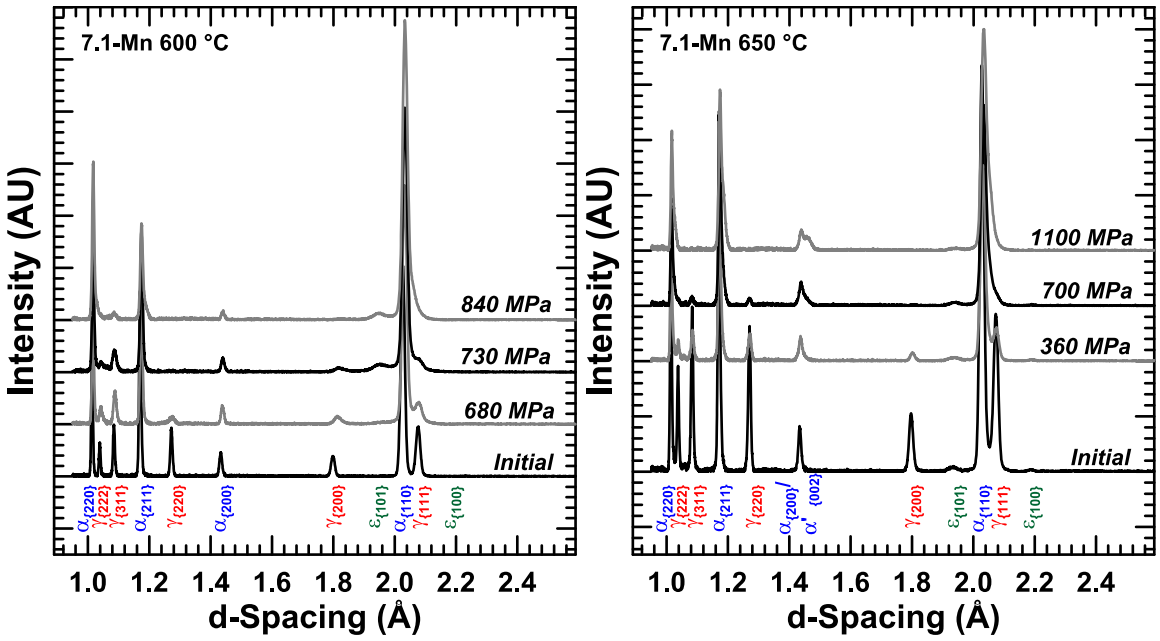

Figure 2 Representative *in situ* neutron diffraction patterns during uniaxial tensile deformation for a) 600 °C and b) 650 °C for 168 hr. Peak indices are indicated on the bottom of the figure. Engineering stresses from the end of each diffraction measurement are indicated on the right side of the figures. Intensity plotted in arbitrary units (AU).

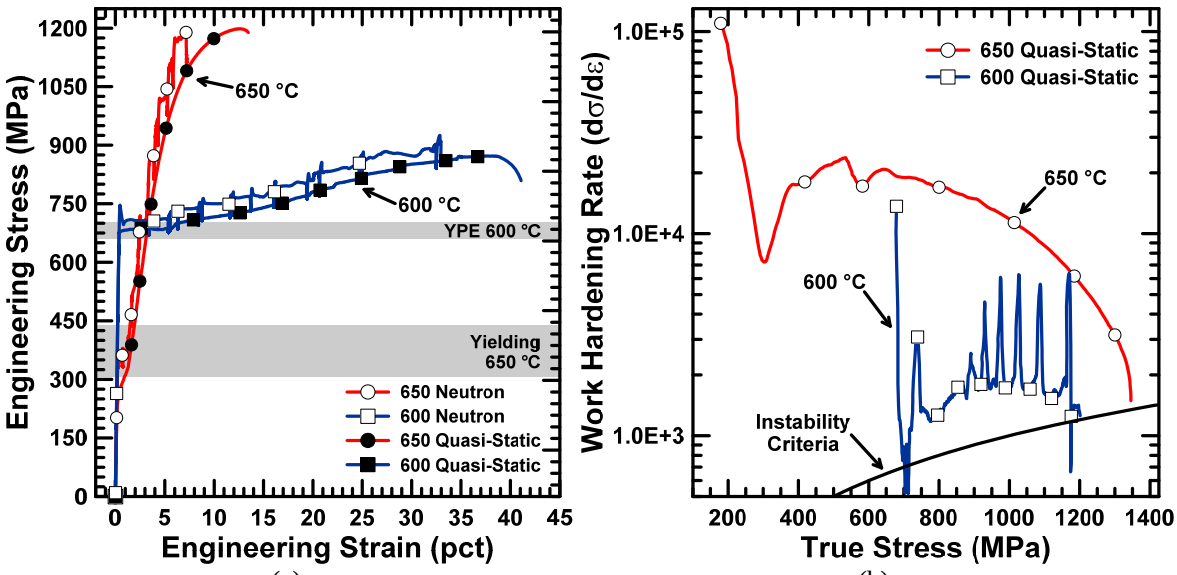

(a) (b)

Figure 3 a) Room temperature tensile engineering stress strain curves for both quasi-static and interrupted neutron *in situ* neutron diffraction samples. Open symbols on the in situ curves correspond to strains for diffraction pattern measurements. b) Instantaneous true work hardening rate ($d\sigma/d\varepsilon$) for the room temperature tested tensile samples. Plotted instability criteria corresponds to the instantaneous work hardening rate equaling the true stress on the sample. Quasi-static tensile tests used a constant engineering strain rate of 5.47×10^{-4} s^{-1} on ASTM E-8 geometry with a 25 mm gauge length.

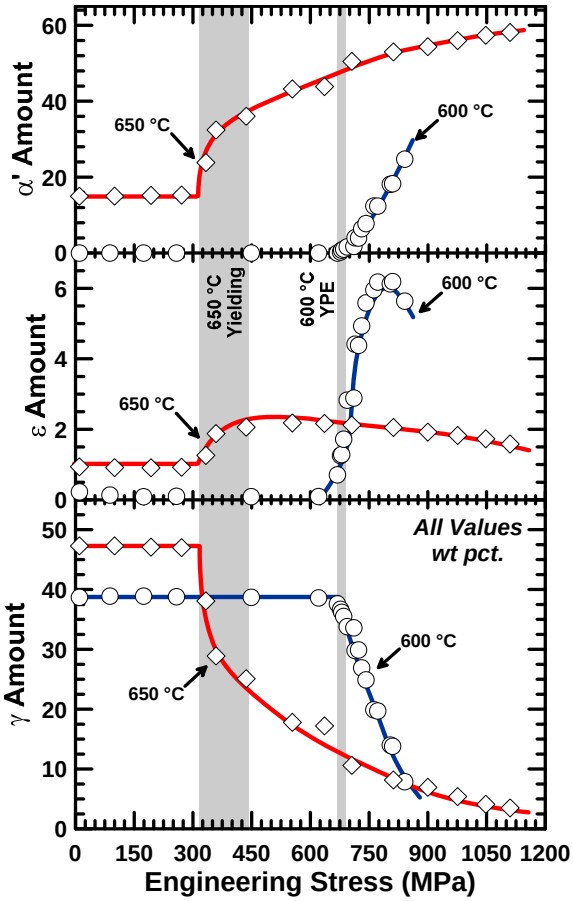

Figure 4 Development of relative austenite, ε, and α' martensite amounts as a function of applied stress for 7.1-Mn steel annealed 168 hr. at the temperatures indicated on the figures. Austenite and ε martensite fractions measured with *in situ* neutron diffraction, α' fraction estimated by subtracting the measured austenite, ε, and intercritical ferrite amounts from 100 pct. Vertical grey bands indicate stresses associated with initial yielding behavior. Uncertainties in the data are typically less than the plotted symbol size.

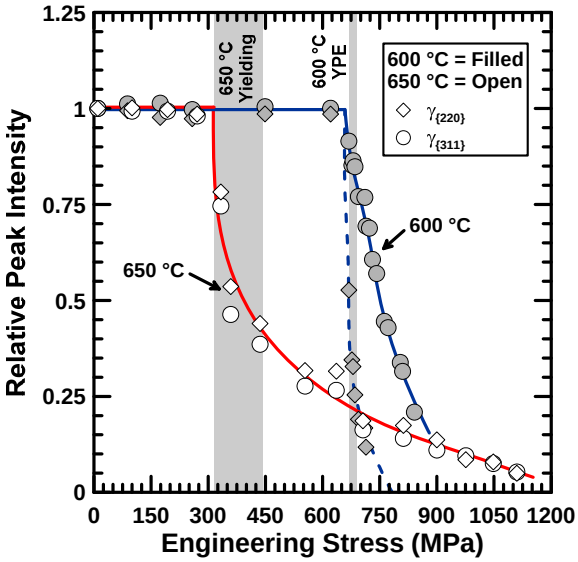

Figure 5 Relative austenite peak intensities for austenite $\gamma_{\{220\}}$ and $\gamma_{\{311\}}$ planes for 600 °C and 650 °C annealed steels with respect to the applied tensile stress in the axial direction as determined by single peak fitting of *in situ* neutron diffraction data. Uncertainties in the data are typically less than the plotted symbol size.

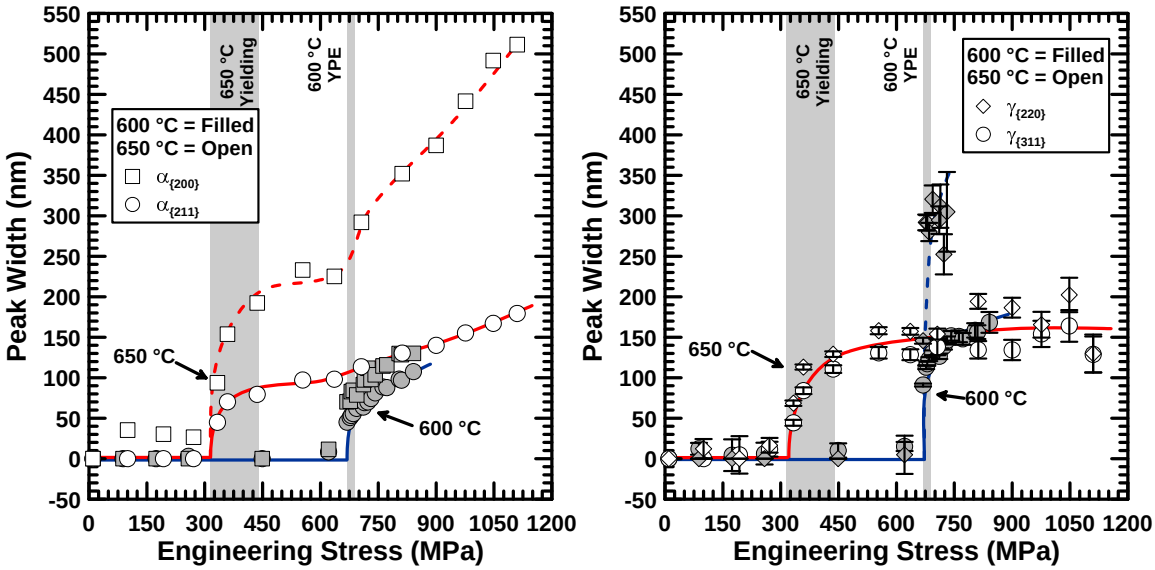

(a) (b)

Figure 6 Instrument corrected peak width for 600 and 650 °C annealed steels with respect to the applied tensile stress in the axial direction as determined by single peak fitting of *in situ* neutron diffraction data for a) ferrite $\alpha_{\{200\}}$ and $\alpha_{\{211\}}$ peaks and b) austenite $\gamma_{\{220\}}$ and $\gamma_{\{311\}}$ peaks. Uncertainties in the data in part a are typically less than the plotted symbol size while uncertainty bars are plotted in part b.

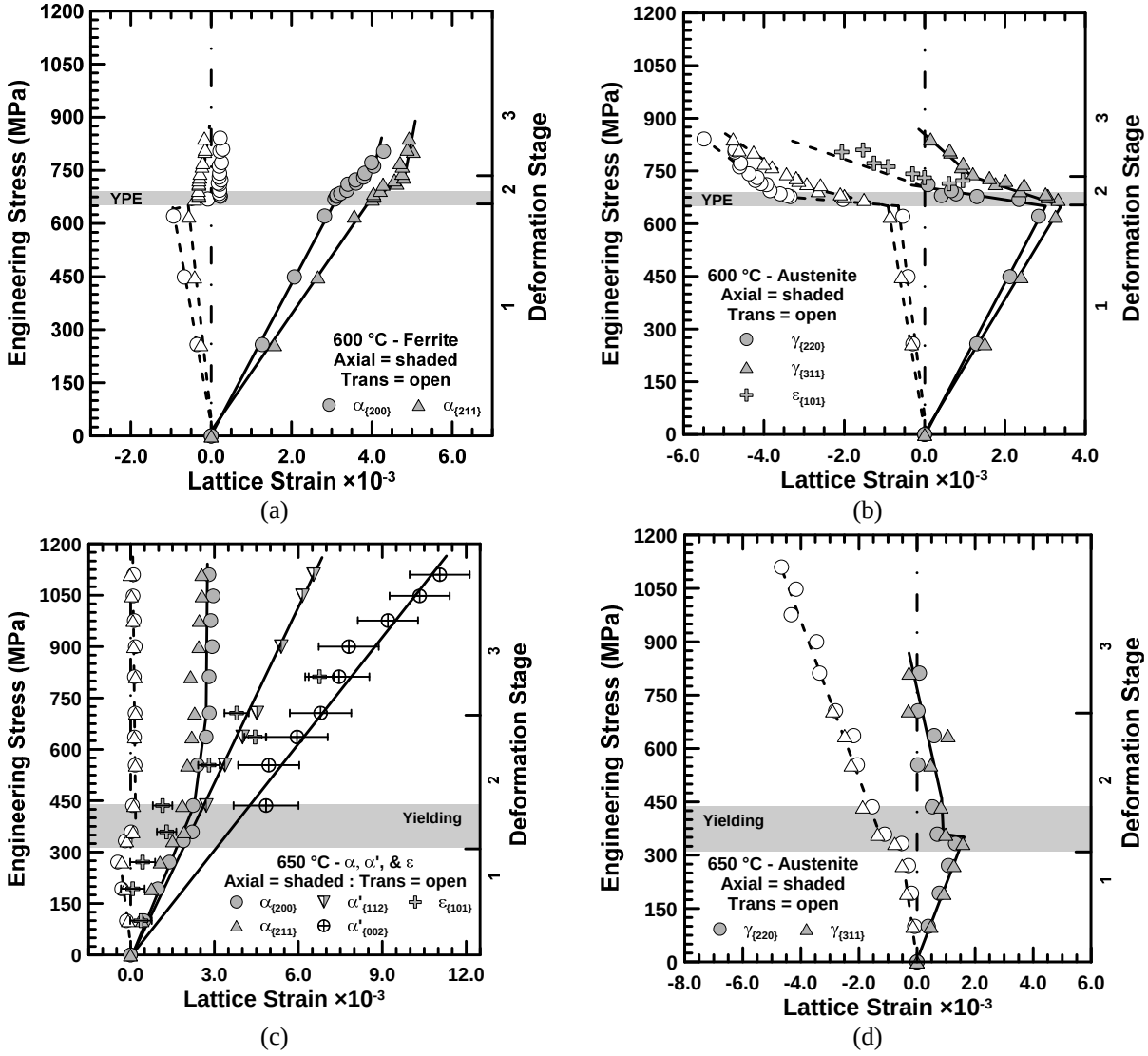

Figure 7 Elastic phase strains for the 7.1-Mn steel annealed at 600 °C for a) ferrite and b) ε martensite and austenite and data from the 650 °C annealed steel for c) ferrite, ε and α' martensite and b) austenite. In each figure lattice strain data for both the axial and transverse directions are plotted with respect to macroscopic tensile stress for 600 °C annealed steel. Uncertainties in the data are typically less than the plotted symbol size except where uncertainty bars are plotted.

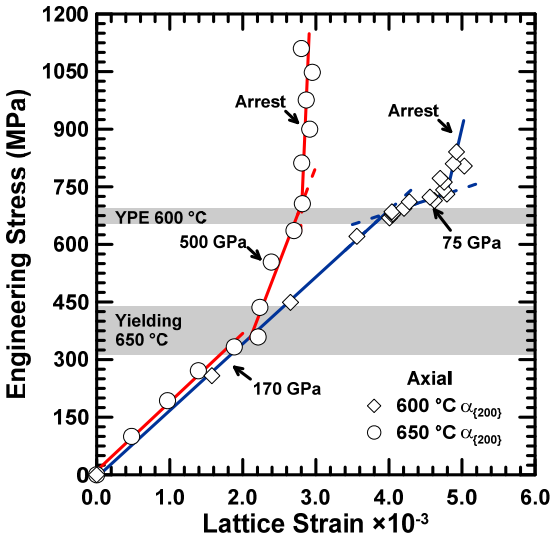

Figure 8 Ferrite $\alpha_{\{200\}}$ lattice strain behavior in the axial diffraction direction as calculated using single peak fitting for the 600 °C and 650 °C annealed steel. Data are replotted from Figure 7a and Figure 7c for clarity. Uncertainties in the data are typically less than the plotted symbol size.

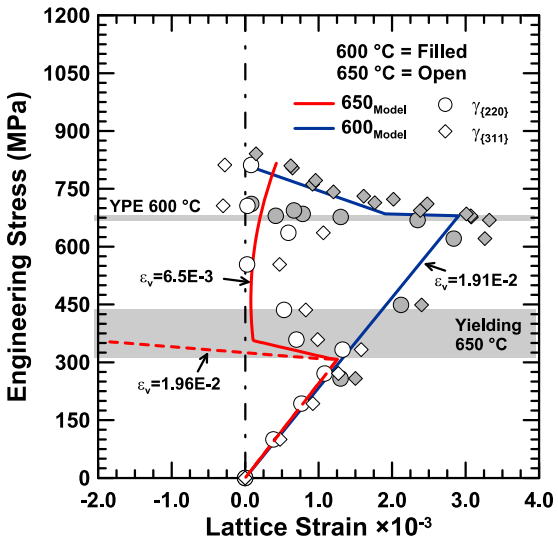

Figure 9 Interpretive model (lines) and observed (points) $\gamma_{\{311\}}$ lattice strains in the axial direction for austenite for the 600 °C and 650 °C annealed steels in the axial and transverse directions. Model calculated using volume strain of $19.1*10^{-3}$ and $7.5*10^{-3}$ for the 600 °C and 650 °C annealed steels, respectively. Uncertainties in the data are typically less than the plotted symbol size.

10.0 TABLES

Table 1 – Predicted Intercritical Austenite Composition

Annealing Temperature (°C)	Austenite Composition (wt pct.)	
	C	Mn
600	0.234	12.9
650	0.153	9.52

Table 2 – Measured and Estimated Lattice Parameters for Ferrite and Austenite [[42–46][47][29]]

Annealing Temperature (°C)	Measured Lattice Parameter (nm)				Estimated Lattice Parameter (nm)		
	Austenite		Ferrite		Austenite	Martensite a	Martensite c
600	0.35942	$\pm 3.9 \times 10^{-6}$	0.28656	$\pm 1.6 \times 10^{-6}$	0.3605	0.2879	0.2880
650	0.35895	$\pm 3.5 \times 10^{-6}$	0.28672	$\pm 1.9 \times 10^{-6}$	0.3602	0.2877	0.2878

Table 3 – Estimated Lattice Strains for Austenite to Martensite Transformation [[42–46] [47][29]]

Annealing Temperature (°C)	$\varepsilon_{1,2}$ (%)	ε_3 (%)	ε_V (%)
600	12.9	-20.1	1.91
650	13.0	-20.1	2.01